Article:

Keylock, C.J. and Nishimura, K. (2016) Wavelet phase analysis of two velocity components to infer the structure of interscale transfers in a turbulent boundary-layer. Fluid Dynamics Research, 48 (2). 021406. ISSN 0169-5983

https://doi.org/10.1088/0169-5983/48/2/021406

Wavelet phase analysis of two velocity components to infer the structure of interscale transfers in a turbulent boundary-layer

Christopher J. Keylock[1a], Kouichi Nishimura[2]

[1]*Sheffield Fluid Mechanics Group and Department of Civil and Structural Engineering, University of Sheffield, Mappin Street, Sheffield, S1 3JD, UK and*

[2] *Graduate School of Environmental Studies, Nagoya University, Furo-cho, Chikusa-ku, Nagoya 464-8601, Japan*

(Dated: March 8, 2016)

Abstract

Scale-dependent phase analysis of velocity time series measured in a zero pressure gradient boundary layer shows that phase coupling between longitudinal and vertical velocity components is strong at both large and small scales, but minimal in the middle of the inertial regime. The same general pattern is observed at all vertical positions studied, but there is stronger phase coherence as the vertical coordinate, y, increases. The phase difference histograms evolve from a unimodal shape at small scales to the development of significant bimodality at the integral scale and above. The asymmetry in the off-diagonal couplings changes sign at the midpoint of the inertial regime, with the small scale relation consistent with intense ejections followed by a more prolonged sweep motion. These results may be interpreted in a manner that is consistent with the action of low speed streaks and hairpin vortices near the wall, with large scale motions further from the wall, the effect of which penetrates to smaller scales. Hence, a measure of phase coupling, when combined with a scale-by-scale decomposition of perpendicular velocity components, is a useful tool for investigating boundary-layer structure and inferring process from single-point measurements.

[a] Corresponding author: c.keylock@sheffield.ac.uk

I. INTRODUCTION

An enhanced understanding of boundary-layer structure is crucial for improving our ability to control and manipulate a variety of environmental and industrial, turbulent flows. An important practical need for such work arises in numerical work, where the use of fully-resolved simulations to the wall is extremely expensive computationally, resulting either in the use of wall-functions to span the gap to the first computational mode, or the use of hybrid methods such as Detached Eddy Simulation [54]. Consequently, there has been a significant amount of experimental research examining the degree of isotropy at inertial and dissipative scales in boundary-layers. These have often focused on very high Reynolds numbers [50] where a clear scale separation can be deemed to hold between the integral and dissipative scales, leading to data that test the applicability of theories developed for homogeneous, isotropic turbulence. Parallel experimental work has investigated and confirmed the basis for the Townsend [57] attached eddy hypothesis [46, 53], leading to revised models for near-wall flow structure [18, 47]. Recent work by de Silva et al. [10] has shown that the attached eddy model can be used to predict the logarithmic dependence of the even-ordered structure functions and that these predictions are borne out in data from experimental and atmospheric flows at a range of Reynolds numbers.

Thus, understanding of boundary-layer processes requires an engagement with the complex inter-scale transfers of energy, vorticity and helicity found in turbulence [27, 33, 49, 58]. Understanding the subtleties of these processes and developing models for them has formed a significant part of the research effort in the field [13, 27, 60]. For example, as alluded to above, the structure function approach to analysing the moments of the velocity increment distribution and their scaling [12] provides a popular means to investigate properties of models for turbulence dissipation and intermittency [29, 52]. More recently, the Caffarelli-Kohn-Nirenberg integral has been used to place bounds on the appropriate form for structure function scaling in the inviscid limit [11]. Alternatively, the structure function, ξ_n, for moment order n may be linked to multifractal methods that characterize the singularity spectrum, $D(\alpha)$, of the sets of non-zero Hölder exponents, α via the Frisch-Parisi conjecture [39, 40]:

$$D(\alpha) = \min_n(\alpha n - \xi_n + 1) \tag{1}$$

In addition to small-scale intermittency, other complications to the classical view of turbulence energy transfer revolve around interscale coupling and the difficulty in viewing large and small scale interactions as independent. For example, the identification of triad interactions [43] complicates the notion of scale separation, while large-scale forcing has been shown to influence the structure of turbulence at smaller scales where classically one would deem the interscale transfers to simply follow Kolmogorov-scaling [38, 64]. More specifically, in the context of boundary-layer flows, the autogenic formation of larger scales of turbulence structure in boundary layers [1] and their organisation into packets [7, 15] has been shown to influence the structure of the smaller scales near the wall [16, 19, 37].

This paper is a technical contribution that demonstrates that measures of phase coherence at a single point, when applied on a scale-by-scale basis using a wavelet transform, reveal how scales are coupled, and provide information on the nature of boundary-layer turbulence structure. Therefore, this approach considers a hierarchy of scales rather than the more common separation into large and small scales using box filters in time/space [8, 16], spectral filtering [14] or wavelets [22]. The wavelet approach provides a natural and consistent means of studying not just the coupling between small and large scales, but relations across a range of consistently defined frequency bands.

II. TECHNIQUES

A. Wavelet analysis

Wavelets have been used extensively in turbulence research. This includes the identification of coherent structures in turbulence data [5, 61, 62], the analysis of the multifractal structure of turbulence by wavelet transform modulus maxima [2, 40], the formulation of randomisation schemes for turbulent inlet boundary condition generation in large-eddy simulations [26] and as a means to examine the formulation of the Navier-Stokes equations themselves [31, 32]. The cross-wavelet spectrum (the wavelet equivalent of the Fourier co-spectrum [4, 6, 21]) has been calculated with the continuous wavelet transform (CWT) for some time [17, 36]. For example, Camussi et al. [6] analysed the cross-wavelet characteristics of pressure signals obtained with microphones at neighbouting locations at the wall in an anechoic wind tunnel. The structure of the observed pressure dipole was related to the presence of near-wall coherent flow structures. In contrast to the use of the CWT, there are advantages in using discrete filter banks in wavelet analyses, and the notion of wavelet cross-covariance and wavelet cross-correlation were introduced in the context of a specific variant of the discrete transform (the Maximal Overlap Discrete Wavelet Transform or MODWT) by Lindsay et al. [35] and formalized by Whitcher et al. [63].

B. The Maximal Overlap Discrete Wavelet Transform (MODWT)

The MODWT is an undecimated transform meaning that, as with the continuous wavelet transform (CWT), N wavelet coefficients, $w_{j,k}$ ($k = 1, \ldots, N$) are generated at each scale, j, for a signal of length N [45]. It can also be applied to any $N \in \mathbb{Z}^+$ while the discrete wavelet transform (DWT) requires that $N = c_w 2^J$, where $j = 1, \ldots, J$ are the wavelet scales up to the largest scale of the decomposition, J, $c_w \in \mathbb{Z}^+$ and, commonly, $c_w = 1$. However, like the discrete wavelet transform (DWT), it is built from a hierarchy of filter banks, giving an exact reconstruction property. In effect, a discrete transform is undertaken for all N circular rotations of a velocity time series, $u(t)$, although effective implementation means that, in practice, the computation is $O(N \log_2 N)$ and not $O(N^2)$ [34]. The MODWT is described in detail by Percival and Walden [45] and is based on a conjugate pair of high and low pass filters which are then scaled proportional to $2^{j/2}$. Efficient implementation uses a periodization of the filters rather than explicit circular convolution and, in this study, a Daubechies least asymmetric wavelet with eight vanishing moments is adopted [9].

Because it is exactly invertible and the energy at each scale is proportional to that in the Fourier amplitude spectrum at the equivalent frequency band (once edge effects are accounted for), the MODWT is an effective analysis tool for turbulence research, particularly regarding synthetic signal generation [25, 26]. In this paper, we study the longitudinal, $u(t)$, and vertical, $v(t)$, velocity components measured in a zero-pressure boundary-layer in a wind tunnel. The MODWT is then applied in turn to $u(t)$ and $v(t)$ to derive the $w^{(u)}_{j_u,k}$ and $w^{(v)}_{j_v,k}$. The cross-phase analysis is then performed over all $k = 1, \ldots, N$ for all wavelet coefficients at a given choice of j_u and j_v.

C. Phase Coupling Measures

The scale-by-scale calculation of phase is performed using the Hilbert transform, which is consistent with an approach taken by Kreuz et al. [30]. We define the analytical signal of $w^{(u)}_{j_u,k}$ as $w^{(u)}_{j_u,k} + i\hat{w}^{(u)}_{j_u,k} = a_{j_u,k}e^{i\phi_{j_u,k}}$, where $\hat{w}^{(u)}_{j_u,k}$ is the Hilbert transform of $w^{(u)}_{j_u,k}$:

$$\hat{w}^{(u)}_{j_u,k} = \frac{1}{\pi}\text{p.v.}\int_{-\infty}^{+\infty} \frac{w^{(u)}_{j_u,k}(\kappa)}{k-\kappa}\,d\kappa \tag{2}$$

and p.v. is the Cauchy principal value. It then follows that the phase is given by

$$\phi^{(u)}_{j_u,k} = \tan^{-1}\frac{\hat{w}^{(u)}_{j_u,k}}{w^{(u)}_{j_u,k}} \tag{3}$$

Hence, given $\phi^{(u)}_{j_u,k}$ and $\phi^{(v)}_{j_v,k}$, the phase difference is

$$\Delta\phi(k) \equiv \Delta\phi_{j_u,j_v|k} = \phi^{(u)}_{j_u,k} - \phi^{(v)}_{j_v,k}. \tag{4}$$

Two summarial measures of phase are adopted. The first is the mean phase coherence [30]: we average the angular distribution of phases on the unit circle in the complex plane:

$$\gamma = \left|\frac{1}{N}\sum_{j=1}^{N} e^{i\Delta\phi(t)}\right| \tag{5}$$

However, the distribution of γ is not uniform, meaning that to check for statistical significance, surrogate values for γ denoted by γ_S are formed by phase-shuffling one of the time series before calculating the phase differences. The mean value, $\bar{\gamma}_S$, is then used to normalize the value of γ from the data:

$$\gamma^* = \begin{cases} 0 & \text{if } \gamma < \bar{\gamma}_S \\ \frac{\gamma-\bar{\gamma}_S}{1-\bar{\gamma}_S} & \text{if } \gamma \geq \bar{\gamma}_S \end{cases} \tag{6}$$

Our second measure is based on an entropic formulation of the information in the phase difference distribution, $\Delta\phi_{j_u,j_v}$. We discretize the interval -2π to $+2\pi$ into $B = 100$ bins (the results converged at $B \sim 60$ dependeing on y and j), and estimate the entropy according to the probability, p in each bin:

$$E = -\sum_{i=1}^{B} p_i \log p_i. \tag{7}$$

In order to facilitate comparison to γ^*, we normalize by the maximum amount of disorder in the distribution, giving $E_I = 1 - (E/E_{\max})$ where $E_{\max} = -\sum_{i=1}^{B}(1/B)\log(1/B)$.

D. Summary of Implementation

We take the MODWT of u, and v, and then align the $w_{j,k}$ at each j for each component based on the support, L_j, of the wavelet. We then calculate γ^* and E_I between all scales

$j_u \in \{1, \ldots, J\}$ and $j_v \in \{1, \ldots, J\}$. Because the support of the wavelet is a function of j, edge effect size is also a function of j and if not accounted for, this will bias analysis [63]. Hence, with $j_{\max} \equiv \max\{j_u, j_v\}$, we correct the calculation of the above measures by using data over $k = L_{j_{\max}} + 1, \ldots, N$ rather than all N samples.

III. EXPERIMENTAL DATA

The velocity data for this paper were obtained for two flow conditions (U_∞ = 6 m s^{-1} and 8 m s^{-1}), with five replicated experiments for each case, in the zero pressure boundary layer wind tunnel at the Cryospheric Environment Simulator at the Shinjo branch of the Nagaoka Institute for Snow and Ice Studies. The wind tunnel has a square cross section of 1 m^2 and a 14 m working section [41]. Experiments were performed over a fixed rough bed (ice coated snow grains) at −10°C. Based on the boundary layer thickness, $\delta \sim 0.2$ m, the dimensionless roughness length, $h/\delta = 0.005$, which is expressed in wall units as $h^+ = hu_*/\nu$ and $h^+ \sim 5.3$ and $h^+ \sim 6.7$ for $U_\infty \in \{6, 8\}$ ms^{-1}, where u_* is the shear velocity and ν is the kinematic viscosity. During each experiment, time series of $N = 2^{17}$ measurements of the longitudinal, u, and vertical, v, velocity were undertaken at eight vertical positions ($y \in \{0.01, 0.02, 0.03, 0.055, 0.07, 0.10, 0.12, 0.15m\}$) at 5 KHz using a Kanomax cross-wire, constant temperature anenometer (model IFA 300 from TSI Inc.) with a 260 KHz response frequency, a length of 1 mm and a width of 5 μ m. Further details on calibration and gain for the wires is provided in Keylock, Nishimura, Nemoto and Ito [23]. Dimensionless distances from the wall for the sample locations are given in terms of wall units ($y^+ = yu_*/\nu$) in Table I. The logarithmic fits to the velocity profiles produced a non-dimensional collapse of the data as seen in Fig. 3a of Keylock, Nishimura and Peinke [24].

The average Taylor Reynolds numbers over the profile for U_∞ = 6 m s^{-1} case was $\mathrm{Re}_\lambda = 205$, while it was $\mathrm{Re}_\lambda = 405$ for U_∞ = 8 m s^{-1}. This increase was a consequence of a constant turbulence intensity (scaling with the mean velocity), but an increase in the estimated mean Taylor length scale from 8 mm to 12 mm with the velocity increase. The extent of the inertial regime was estimated from the limits to the power-law scaling of the third order structure function and its upper limit equated to $\ell \sim 1000$ samples on average. This can be seen in an alternative fashion, from the mean Fourier amplitude spectrum, in Fig. 1, which shows the well-developed scaling region in the data. With $N = 2^{17}$, a value of $J = 13$ was selected, at which our wavelet has an effective support of $L_J = 2^{15.8}$. These wavelet scales are superimposed on Fig. 1 and it is clear that the low frequency limit of the scaling region lies in the interval $7 < j < 8$.

IV. RESULTS

Results for γ^* at $y = 0.55$ m ($y^+ = 280$) and $U = 6$ m s^{-1} are shown in Fig. 2. Our color scheme is such that if $\gamma < \bar{\gamma_S}$ (i.e. results are insignificant), they are shown in white, with otherwise a linear evolution from dark to lighter shades. For each of the J^2 cells, we extracted the minimum, median, and maximum values for γ^* over the five replicates, and these form panels (a) to (c) in Fig. 2. For all cases, it is the results along the diagonal that have the greatest significance but at both small and large scales there are significant couplings off the diagonal, which 'pinch off' at $j = 4, 5$ i.e. the mid-point of the scaling regime from Fig. 1. Note that there is strong connectivity between velocity components at large scales and although this is reduced from $j = 7, 8$ down to $j \sim 4$, it is still significant [20]. Interscale connectivity for boundary-layer flows in terms of an amplitude modulation of the small scales by the large has recently been considered in some detail [14, 16, 37] and evidence for interscale connectivity is readily apparent in Fig. 2. For the majority of the rest of the paper we focus on the results on the diagonal (i.e. the phase coherence between the two velocity components at a given scale). We explain the observed pattern in terms of an evolution of the probability distributions for phase as a function of j.

The median values for γ^*, i.e. $[\gamma^*]_{50}$, along the diagonal $j_u = j_v$ are shown in the top two panels in the left column of Fig. 3. It is clear that the pattern seen in Fig. 2 occurs for both U and all y. Furthermore, the results for E_I (bottom panels on the left of Fig. 3) are very similar to those for $[\gamma^*]_{50}$. Figure 4 checks the convergence of the results for $[\gamma^*]_{50}$ on the diagonal ($j_u = j_v$) as a function of the sample size, N over which the values are estimated for the $U_\infty = 6$ m s^{-1} dataset (up to the full length of the dataset, $N = 2^{17}$ samples). Each panel is for a separate j, and the eight lines in each panel are for different y. Hence, the right-hand values in each panel are those shown as lines in Fig. 3a. Thus, the very similar, small values for $[\gamma^*]_{50}$ at $j = 4$ in Fig. 3a, are reflected in the barely differentiable lines in the $j = 4$ panel of Fig. 4. The use of a log abscissa underplays the quality of the convergence, which is shown for a subset of six of the thirteen values for j in Fig. 5 using a linear abscissa.

While convergence takes longer for greater j (as anticipated, owing to the wider support of the wavelet filter at this scale), by $N = 2^{15}$ samples (i.e. a quarter the number used in analysis) there is only a minor variation in the values obtained even at $j = 13$. Hence, the results shown in Fig. 3 and hereafter may be deemed to be sufficiently precise to permit comparisons as a function of y and j at the very least for $j \leq 12$.

A. Inner and Outer Boundary-Layer Behavior

Figure 3 shows stronger phase coherence (less disorder) for high j, attains a minimum in the center of the scaling range and then increases again as one moves towards λ. The data in Fig. 3 are plotted such that lines become more solid, and the color changes from black to red as the y-coordinate of the measurements increases. It is clear that there is stronger phase coherence further from the wall, but that otherwise the pattern is similar for all y, with the exception that close to the wall, the coherence minimum is expressed at somewhat smaller scales. The differences seen in the left-hand panels of Fig. 3 are too small to attempt a collapse with y or y^+. Hence, the right-hand panels examine scaling with Taylor Reynolds number, $\mathrm{Re}_\lambda(y)$, in panels (e) and (f), and local mean velocity $\langle u(y) \rangle$ in (g) and (h). Note that because of the decrease in u'^2 with increasing y, normalization with $\mathrm{Re}_\lambda(y)$ is expressed as a product. Results as a function of $\mathrm{Re}_\lambda(y)$ collapse better for $U = 6$ ms^{-1} in Fig. 3e than $U = 8$ ms^{-1} in Fig. 3(f), and this additional U-dependence suggests that scaling on inner variables is less physically relevant than using $\langle u(y) \rangle$.

While the curves in Fig. 3(a) and 3(b) exhibit an approximate random variation about the trend, in Fig. 3(e)-3(h), there is a more systematic y dependence, with the bottom three measurements ($y \leq 0.03$ m) exhibiting a higher phase coherence at intermediate scales, and all measurements for greater y collapsing onto the same curve. A value of $y = 0.03$ m corresponds to $y^+ = 151$ to 154 wall units over the five replicates ($U = 6$ m s^{-1}) and $y^+ = 191$ to 194 for $U = 8$ m s^{-1}. The next sample vertically is at $y = 0.055$ m, which for $U = 6$ m s^{-1}, equates to $y^+ = 280$. Ganapathisubramani et al. [15] showed that organized hairpin-like structures are responsible for a significant proportion of the total Reynolds stress at $y^+ \leq 150$. However, for $y^+ \geq 200$, while various coherent structures existed, there was no evidence for long, low speed streaks, or other wall-related structures. Hence, the differences observed here appear to relate to the physical basis for the standard separation between the lower and upper parts of the outer layer at $y^+ \sim 200$, with the important role of coherent structures near the wall evident in the greater phase coherence in that region.

B. Distributions for $\Delta\phi(t)$

A preliminary inspection of the histograms for $\Delta\phi(t)$ revealed a tendency towards a bimodal response at large j. Hence, making use of the fact that the fourth standardized moment of a distribution (the normalized flatness or kurtosis) has a lower bound given by the squared skewness plus one [44], Sarle's multimodality coefficient, b, for a variable, u, is given by

$$b(u) = \frac{S(u)^2 + 1}{K(u) + \frac{3(N-1)^2}{(N-2)(N-3)}}$$

$$K(u) = \frac{\sum_{i=1}^{N}(u - \overline{u})^4/N}{\sigma(u)^4} - 3 \tag{8}$$

where S is the sample skewness, K is the sample excess kurtosis, where the subtraction adjustment yields a value of 0 for a Gaussian distribution, N is the sample size, and σ is the standard deviation. Values for the multimodality coefficient are shown in Fig. 6 as a function of U, y, and j, where the symbols indicate the median value and the vertical bars about these symbols (which are barely visible, except at small j in some panels) indicate the range of values for the replicated experiments. The dotted, horizontal line at $b = 5/9$ shows the expected value for both a uniform and an exponential distribution. For b to exceed these values, the kurtosis must be excessive. There are three primary features in Fig. 6:

1. The general increase in b with j, with a peak occurring at $j \sim 10$, followed by a plateauing or a decrease;

2. The increase in maximum values for b as y increases, with the data nearest the wall failing to exhibit clear multimodality for any j; and,

3. A reduced propensity for significant multimodality at small j as U increases.

Given the low errors across the replicates in Fig. 6, the median results were deemed representative and the median phase difference ($[\Delta\phi(t)]_{50}$) histograms for all j, U and y are shown in Fig. 7. The results are very similar for both input velocities, with any slight differences either due to experimental error or the fact that y has been used for the plotting (to permit two lines in the same panel) rather than the more dynamically relevant, dimensionless, wall unit-based vertical coordinate, y^+.

For $j < 4$ the phase differences have a clear, single mode positioned at $\Delta\phi(t) \sim -\pi/6$, highlighting the v - u, ejection-sweep structure. The increase in b through $j = 4$ to $j = 8$ is due to a movement of the mode towards zero phase lag, a flattening of this mode as the distribution tends towards uniform probability within $-\pi < \Delta\phi(t) < +\pi$, followed by the emergence of two modes at the edge of the flattened part of the histogram by $j = 7$. These modes at $|\Delta\phi(t)| \lesssim \pi$ become ever more clearly expressed as $j \to J$. At $y = 0.02$ m it is clear for $j = 5, \ldots, 8$ that the negative $\Delta\phi(t)$ peak initially dominates, while for $j = 9, \ldots, 13$ there is a transition to the positive peak. In contrast, the negative $\Delta\phi(t)$ peak dominates for $j = 9, \ldots, 13$ at $y = 0.15$ m. Hence, the large-scale structure in a boundary-layer alters in nature between the inner and outer regions, with two modal responses present in both, but a difference in their relative frequency occurring.

These differences can be analysed by considering the derivative skewness of $\Delta\phi(t)$, which leads to changes in the behavior of the zero-crossings of the signal. Study of the zero crossings of turbulence data [55] and investigation of the (fractal) properties thereof has a history that dates back to Kolmogorov [28]. Indeed, the quantity describing the scaling of the zero-crossings has subsequently been termed the Kolmogorov Capacity [25, 42, 59]. Here, we consider changes in the skewness by the difference in the spacing in time of the zero-crossings ($\Delta(t)^{(Z0)}$) for positive to negative crossings ($\Delta(t)^{(Z0)}_{(+-)}$) and negative to positive crossings ($\Delta(t)^{(Z0)}_{(-+)}$). Based on the results in Fig. 7, we focus on $j = 10$ and consider the flow near the wall ($z = 0.01$ m) and in the outer layer ($z = 0.15$ m), which for $U = 6$ ms^{-1} equate to $y^+ = 50$ and $y^+ = 765$, respectively. The histograms in Fig. 8 show that there is no real difference in $\Delta(t)^{(Z0)}_{(+-)}$ at either height and that $\Delta(t)^{(Z0)}_{(-+)}$ is very similar to $\Delta(t)^{(Z0)}_{(+-)}$ at $y^+ = 765$. That these similar marginal distributions result in a correlated structure for $y^+ = 765$ is clear in the bottom right figure - a longer time between a negative crossing to a positive crossing is correlated ($R = 0.31$) to the time between a positive crossing to a negative crossing. In contrast, and as seen in the top-right panel, near the wall, $\Delta(t)^{(Z0)}_{(-+)}$ is very differently distributed, with no clear mode and a much longer tail than the other cases (despite the fact that near the wall, typical timescales for turbulence are shorter). This results in a decorrelation between $\Delta(t)^{(Z0)}_{(-+)}$ and $\Delta(t)^{(Z0)}_{(+-)}$ as shown in the bottom-left scatterplot of Fig. 8. The similarity of the marginals, and the significance covariance in the joint distribution at $y^+ = 765$, means that a model for the phase difference histogram at this height is one where the signal has some asymmetry (the mode for $\Delta(t)^{(Z0)}_{(+-)}$, the time spent in the $\Delta\phi(t) < 0$ state, is a little longer than for $\Delta(t)^{(Z0)}_{(+-)}$) and periods of positive phase coherence are coupled to periods of negative coherence. For $y^+ = 50$, while the duration distribution in the $\Delta\phi(t) < 0$ state is similar, the distribution for $\Delta(t)^{(Z0)}_{(-+)}$ has a longer tail, resulting in more time spent in the $\Delta\phi(t) > 0$ state on average. This interpretation is consistent with the differences in mass either side of $\Delta\phi(t) = 0$ in Fig. 7 but provides greater information on the structure. Specifically, the decoupling (correlation coefficient, $R = 0.08$) at $y^+ = 50$ means that the extended $\Delta\phi(t) > 0$ events are approximately independent of the $\Delta\phi(t) < 0$ cases. That this is a near-wall phenomenon is clear in Fig. 7 where the tendency for greater mass in the positive mode of the histogram at large j has disappeared by $y = 0.055$ m ($y^+ = 280$ for $U = 6$ ms^{-1}).

C. Asymmetry in the Interactions

We define an asymmetry measure for the off-diagonal interactions involving γ^* as

$$A^{\gamma}_{j_u,j_v} = \frac{[\gamma^*_{j_u,j_v}]_{50} - [\gamma^*_{j_v,j_u}]_{50}}{\frac{1}{2}([\gamma^*_{j_u,j_u}]_{50} + [\gamma^*_{j_v,j_v}]_{50})} \tag{9}$$

Because of the symmetry of $|A^{\gamma}_{j_u,j_v}|$, we plot results for $U = 6$m s^{-1} and $U = 8$m s^{-1} in the lower and upper halves, respectively, of the panels in Fig. 9. There is a more pronounced asymmetry for the fine scales, with the results at ($j_u = 2, 3,\ j_v = 3, 2$) particularly marked. Results are consistent for both U and different y, with a change in the sign of $A^{\gamma}_{j_u,j_v}$ close to the diagonal occurring at $j \sim 5$, i.e. the middle of the inertial range, and increasing to $j = 6$ for $y = 0.15$m. For $j < 5$, larger scales for u are more strongly coupled to smaller scales for v on average, with the opposite the case for larger j. Note that the small j behavior is also consistent with a hairpin model of short-term, intense ejections, coupled to and followed by a more sustained sweeping motion. At the larger scales, the vertical advection of packets of hairpins [1] that have a local longitudinal velocity similar to the background velocity field, such that variations in u are induced by the vorticity of the structures themselves, would explain the coupling between longer duration vertical movements and shorter duration changes in u.

V. CONCLUSION

Both measures of phase coherence, when applied on a scale-by-scale basis, revealed similar features of a turbulent boundary-layer from measurements of velocity at a single point. Given that $L_{j=1}$ in this study is $\simeq \lambda$, and $L_{j=7} \simeq \ell$, the distinct zones in Fig. 2 correspond to (with lengths derived for the $U = 8$ ms^{-1} case):

1. $1 \leq j \leq 4$ (0.01 m to 0.17 m): Inertial regime with growing coherence as one moves from large to small scales;

2. $4 \leq j \leq 6$ (0.17 m to 0.485 m): Inertial regime with only weak phase-coupling to smaller scales;

3. $j > 6$: (> 0.485 m): The upper part of the inertial regime and then very large scale motions (VSLMs) [1] with significant phase coherence across scales.

This pattern persists for all y, meaning that the effect of the VSLMs effects the smaller scales [14, 16] and persists down towards the wall [37]. However, near the wall there is greater coherence than anticipated relative to the local mean velocity (attempted collapse on the right-hand side of Fig. 3). This enhanced organization reflects the presence of near-wall streaks and hairpin-like structures.

The significant phase coupling between virtually all j in the high frequency end of the scaling region for the dynamics ($j \lesssim 5$) is consistent not only with a "hand-to-hand" transfer of energy [48], but correlated behavior across scales [3], with the phase asymmetry, $A^{\gamma}_{j(u),j(v)}$ indicating that higher frequency (low j) variability in v is more strongly coupled to larger scale, lower frequency variation in u than vice versa. Similar multiscale coupling is seen at the largest scales in both Fig. 2 and Fig. 9, particularly in the nearer wall locations in Fig. 9. This implies that there are two scales to turbulence energy transfer, with the middle of the inertial region acting as a (permeable) barrier to continuous transfer. Hence, this study provides some evidence to support traditonal scale-separation arguments in turbulence [56] and the rationale behind the definition of subfilter scales in large-eddy simulations [51] but it also highlights that this is an approximation and that large scales leave an imprint on smaller scales in boundary-layers. [24, 37, 38, 43, 64].

---

[1] Adrian R J, Meinhart C D and Tomkins C D 2000 *J. Fluid Mech.* **422**, 1–54.

[2] Arnéodo A, Manneville S, Muzy J F and Roux S G 1999 *Phil. Trans. R. Soc. Lond. A* **357**, 2415–2438.

[3] Betchov R 1976 *Archives Mechanics* **28**(5-6), 837–845.

[4] Bos W, Touil H, Shao L and Bertogli J 2004 *Phys. Fluids* **16**, 3818–3823.

[5] Camussi R and Guj G 1997 *J. Fluid Mech.* **348**, 177–199.

[6] Camussi R, Robert G and Jacob M C 2008 *J. Fluid Mech.* **617**, 11–30.

[7] Christensen K T and Adrian R J 2001 *J. Fluid Mech.* **431**, 433–443.

[8] Chung D and McKeon B J 2010 *J. Fluid Mech.* **661**, 341–364.

[9] Daubechies I 1992 *Ten Lectures on Wavelets* SIAM, Philadelphia.

[10] de Silva C M, Marusic I and Woodcock J D 2015 *J. Fluid Mech.* **769**, 654–686.

[11] Dowker M and Ohkitani K 2012 *Phys. Fluids* **24**(115112).

[12] Frisch U and Parisi G 1985 *in* M Ghil, R Benzi and G Parisi, eds, 'Turbulence and Predictability in Geophysical Fluid Dynamics and Climate Dynamics' North Holland pp. 84–88.

[13] Frisch U, Sulem P L and Nelkin M 1978 *J. Fluid Mech.* **87**, 719–736.

[14] Ganapathisubramani B, Hutchins N, Monty J P, Chung D and Marusic I 2012 *J. Fluid Mech.* **712**, 61–91.

[15] Ganapathisubramani B, Longmire E K and Marusic I 2003 *J. Fluid Mech.* **478**, 35–46.

[16] Guala M, Metzger M and McKeon B J 2011 *J. Fluid Mech.* **666**, 573–604.

[17] Hudgins L, Friehe C A and Mayer M E 1993 *Phys. Rev. Lett.* **71**, 3279–3282.

[18] Hultmark M 2012 *J. Fluid Mech.* **707**, 575–584.

[19] Hutchins N and Marusic I 2007 *Phil. Trans. R. Soc. A* **365**, 647–664.

[20] Katul G G, Angelini C, De Canditiis D, Amato U, Vidakovic B and Albertson J D 2003 *Geophys. Res. Lett.* **30**(4).

[21] Katul G G, Porporato A, Manes C and Meneveau C 2013 *Phys. Fluids* **25**, 091702.

[22] Keylock C J, Ganapathasubramani B, Monty J, Hutchins N and Marusic I 2016 *Fluid Dyn. Res.* .

[23] Keylock C J, Nishimura K, Nemoto M and Ito Y 2012 *Environ. Fluid Mech.* **12**, 227–250.

[24] Keylock C J, Nishimura K and Peinke J 2012 *J. Geophys. Res.* **117**.

[25] Keylock C J, Stresing R and Peinke J 2015 *Phys. Fluids* **27**, 025104.

[26] Keylock C J, Tokyay T E and Constantinescu G 2011 *J. Turbul.* **12**, N45.

[27] Kolmogorov A N 1941 *Dokl. Akad. Nauk. SSSR.* **30**, 299–303.

[28] Kolmogorov A N 1958 *Dokl. Akad. Nauk. SSSR.* **119**, 861–864.

[29] Kolmogorov A N 1962 *J. Fluid Mech.* **13**, 82–85.

[30] Kreuz T, Mormann F, Andrzejak R G, Kraskov A, Lehnertz K and Grassberger P 2007 *Physica D* **225**, 29–42.

[31] Lewalle J 2000 *J. Turbul.* **1**, N4.

[32] Lewalle J 2010 *Physica D* **239**, 1232–1235.

[33] Li Y and Meneveau C 2005 *Phys. Rev. Lett.* **95**(164502).

[34] Liang J and Parks T W 1996 *IEEE Trans. Sig. Proc.* **44**, 225–232.

[35] Lindsay R W, Percival D B and Rothrock D A 1996 *IEEE Trans. on Geosci. and Remote Sens.* **3**, 771–787.

[36] Liu P C 1994 *in* E Foufoula-Georgiou and P Kumar, eds, 'Wavelets and Geophysics' Academic Press, San Diego, Ca pp. 151–166.

[37] Marusic I, Mathis R and Hutchins N 2010 *Science* **329**, 193–196.

[38] Mazellier N and Vassilicos J C 2008 *Phys. Fluids* **20**(015101).

[39] Meneveau C and Sreenivasan K 1991 *J. Fluid Mech.* **224**, 429–484.

[40] Muzy J F, Bacry E and Arnéodo A 1991 *Phys. Rev. Lett.* **67**, 3515–3518.

[41] Nemoto M and Nishimura K 2001 *Boundary-Layer Meteorol.* **100**, 149–170.

[42] Nicolleau F and Vassilicos J C 1999 *Phil. Trans. R. Soc. Lond., Ser. A* **357**, 2439–2457.

[43] Ohkitani K and Kida S 1992 *Phys. Fluids A* **4**, 794–802.

[44] Pearson K 1929 *Biometrika* **21**, 370–375.

[45] Percival D B and Walden A T 2000 *Wavelet Methods for Times Series Analysis* Cambridge University Press Cambridge, U.K.

[46] Perry A E and Li J D 1990 *J. Fluid Mech.* **218**, 405–438.

[47] Perry A E and Marusic I 1995 *J. Fluid Mech.* **298**, 361–388.

[48] Richardson L F 1922 *Weather Prediction by Numerical Process* Cambridge University Press.

[49] Richardson L F 1926 *Proc. R. Soc. London Ser. A* **110**, 709–737.

[50] Saddoughi S G and Veeravallit S V 1994 *J. Fluid Mech.* **268**, 333–372.

TABLE I. The vertical coordinates, y for data acquisition, expressed in wall units, y^+, for the two choices for U_∞.

y (m)	y^+ ($U_\infty = 6$ ms^{-1})	y^+ ($U_\infty = 8$ ms^{-1})
0.010	50.8	64.4
0.020	101.6	128.8
0.030	152.4	193.2
0.055	279.4	354.1
0.070	355.6	450.7
0.100	508.1	643.8
0.120	609.7	772.6
0.150	762.1	965.8

[51] Sagaut P 2006 *Large Eddy Simulation for Incompressible Flows* Springer.

[52] She Z S and Leveque E 1994 *Phys. Rev. Lett.* **72**, 336–339.

[53] Sillero J A, Jiménez J and Moser R D 2013 *Phys. Fluids* **25**, 105102.

[54] Spalart P R, Deck S, Shur M L, Squires K D, Strelets M K and Travin A 2006 *Theoretical and Computational Fluid Dynamics* **20**(3), 181–195.

[55] Sreenivasan K R, Prabhu A and Narasimha R 1983 *J. Fluid Mech.* **137**, 251–272.

[56] Tennekes H and Lumley J L 1972 *A First Course in Turbulence* M.I.T. Press.

[57] Townsend A A 1976 *The Structure of Turbulent Shear Flow* Cambridge University Press.

[58] Vassilicos J C 2015 *Ann. Rev. Fluid Mech.* **47**, 95–114.

[59] Vassilicos J C and Hunt J C R 1991 *Proc. R. Soc. Lond. A* **435**, 505–534.

[60] von Karman T and Howarth L 1938 *Proc. R. Soc. London, Ser. A* **164**, 192.

[61] Watanabe T, Sakai Y, Nagata K, Ito Y and Hayase T 2014 *Phys. Fluids* **26**(9).

[62] Wesson K H, Katul G G and Siqueira M 2003 *Boundary-Layer Meteorol.* **106**(3), 507–525.

[63] Whitcher B, Guttorp P and Percival D B 2000 *J. Geophys. Res.* **105**(D11), 14941–14962.

[64] Yeung P K and Brasseur J G 1991 *Phys. Fluids A* **3**, 884–897.

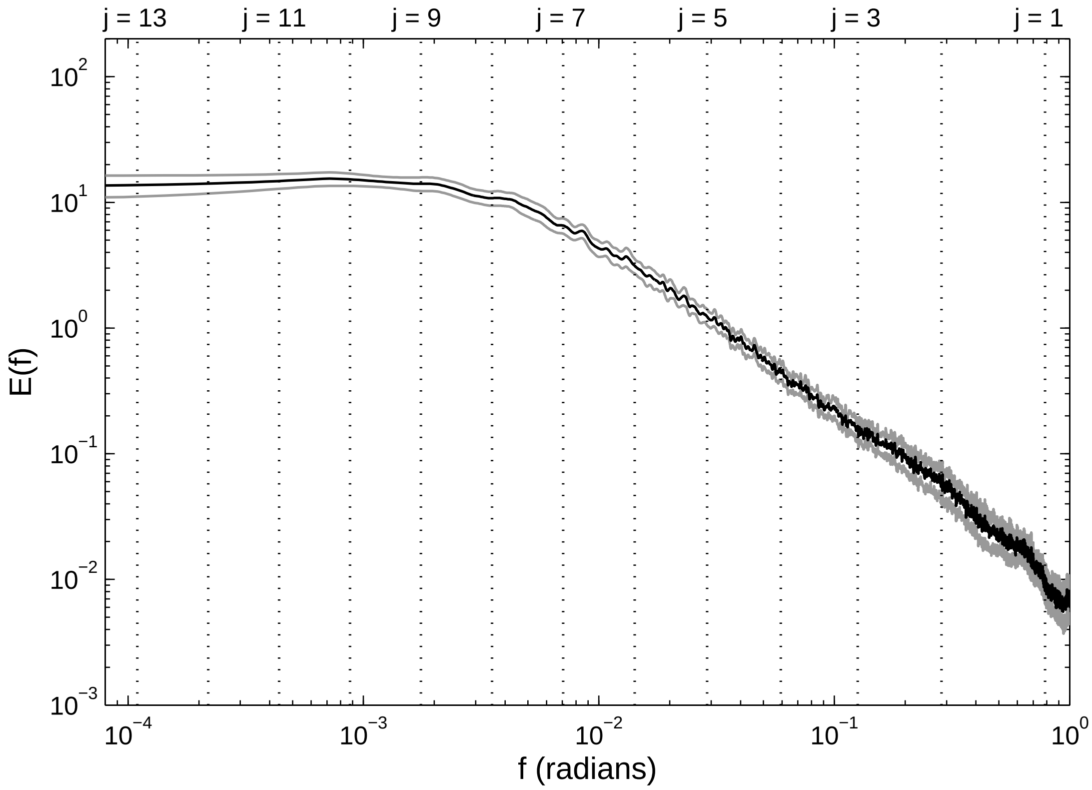

FIG. 1. The mean Fourier amplitude spectrum for the data in this study (black), with 95% confidence intervals based on the standard error (gray lines) also shown. The vertical dotted lines show the equivalent frequencies of the wavelet scales used in the study.

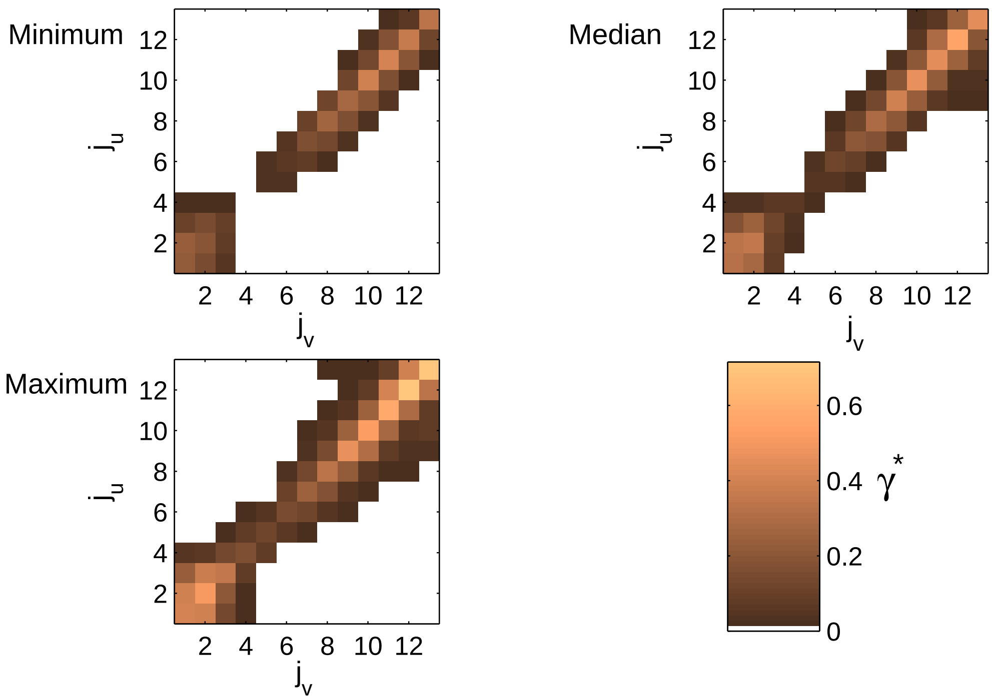

FIG. 2. The minimum, median and maximum values for γ^* at each $\{j_v, j_u\}$ combination over the five replicates for the data obtained at $y = 0.055$ m ($y^+ = 279$) with $U = 6$ m s^{-1}. All are plotted on the same color scheme, with results for $\gamma^* < \bar{\gamma_S}$ shown in white.

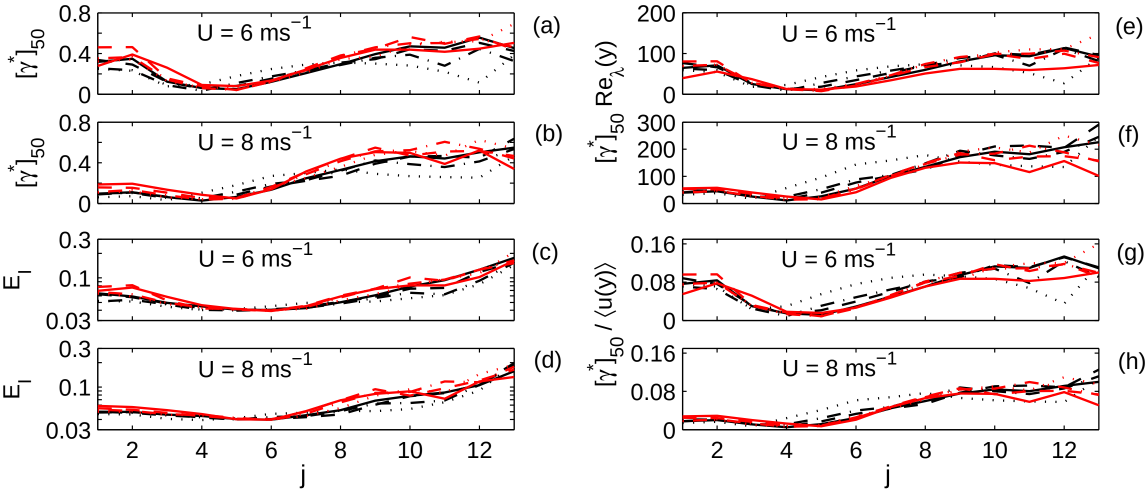

FIG. 3. Values for $[\gamma^*]_{50}$, (a) and (b), and E_I (c) and (d), along the diagonal of the scale-by-scale decomposition (i.e. $j_u = j_v$) for U = 6 m s^{-1}, (a) and (c), and U = 8 m s^{-1}, (b) and (d). Given their similarity, $[\gamma^*]_{50}$ is then normalized by the local Taylor Reynolds number, $\mathrm{Re}_\lambda(y)$, in (e) and (f), and the local mean longitudinal velocity, $\langle u(y)\rangle$ in (g) and (h), with U = 6 m s^{-1} in (e) and (g), and U = 8 m s^{-1} in (f) and (h). Each line on each panel plot corresponds to the median results at a given y according to: y = 0.01 m (black, dotted); y = 0.02 m (black, dot-dashed); y = 0.03 m (black, dashed); y = 0.055 m (black, solid); y = 0.07 m (red, dotted); y = 0.10 m (red, dot-dashed); y = 0.12 m (red, dashed); and, y = 0.15 m (red, solid).

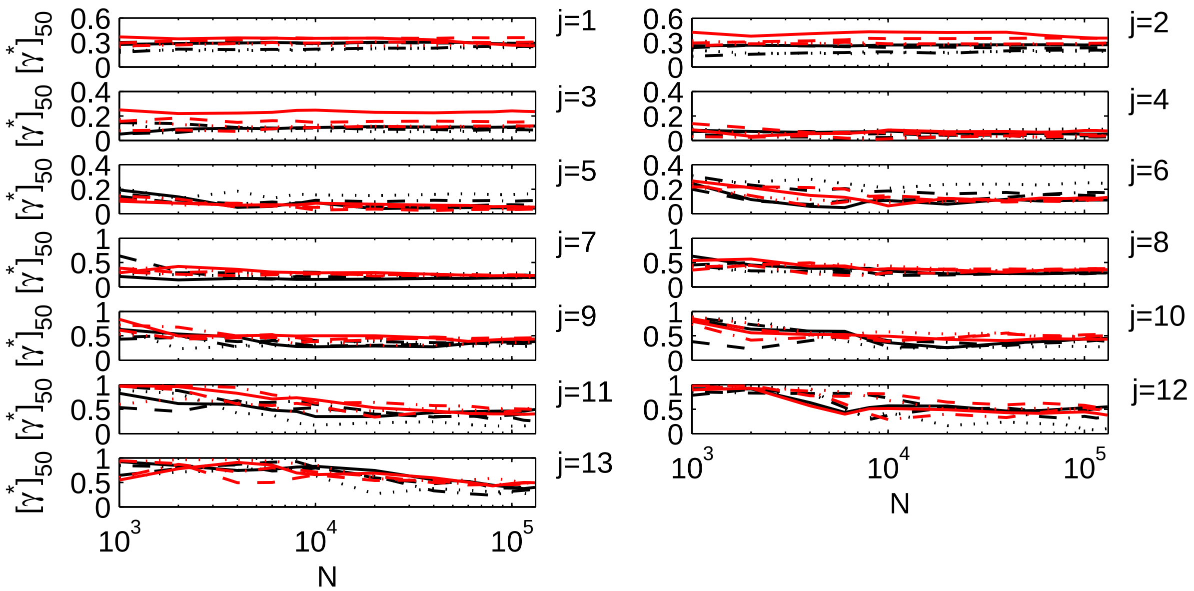

FIG. 4. Values for $[\gamma^*]_{50}$ obtained at the thirteen values for j ($j_u = j_v$) for $U = 6$ m s^{-1}. Results are shown as a function of sample length, N, indicating the convergence of the results by $N = 2^{17}$ samples. Each line on each panel corresponds to: $y = 0.01$ m (black, dotted); $y = 0.02$ m (black, dot-dashed); $y = 0.03$ m (black, dashed); $y = 0.055$ m (black, solid); $y = 0.07$ m (red, dotted); $y = 0.10$ m (red, dot-dashed); $y = 0.12$ m (red, dashed); and, $y = 0.15$ m (red, solid).

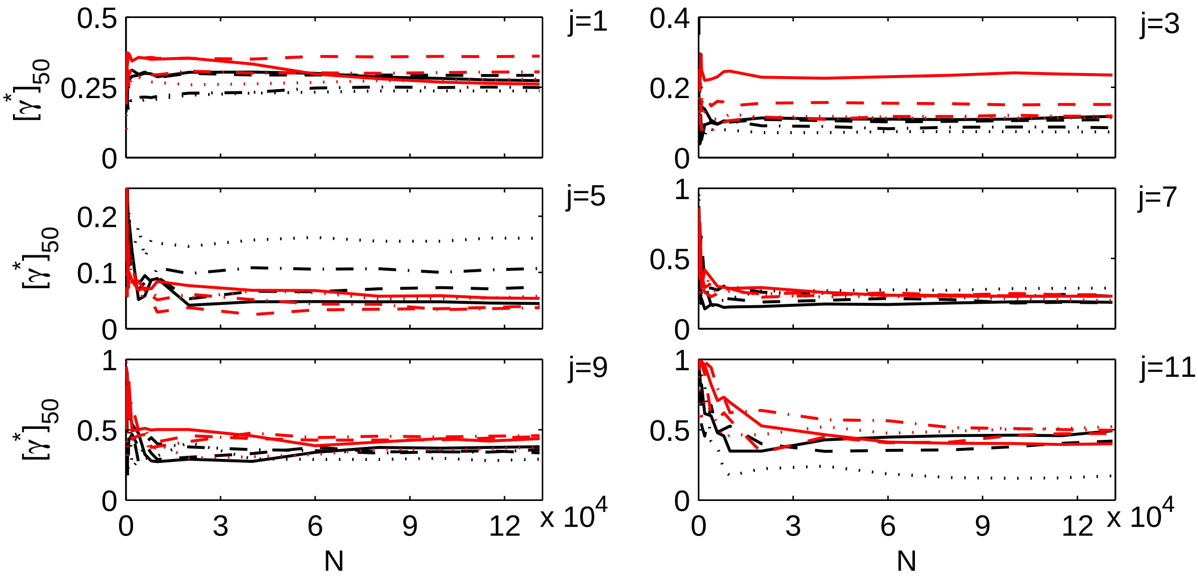

FIG. 5. Values for $[\gamma^*]_{50}$ obtained at six values for j at U = 6 m s^{-1}. Results are shown as a function of sample length, N, indicating the convergence of the results by $N = 2^{17}$ samples. Each line on each panel corresponds to: y = 0.01 m (black, dotted); y = 0.02 m (black, dot-dashed); y = 0.03 m (black, dashed); y = 0.055 m (black, solid); y = 0.07 m (red, dotted); y = 0.10 m (red, dot-dashed); y = 0.12 m (red, dashed); and, y = 0.15 m (red, solid).

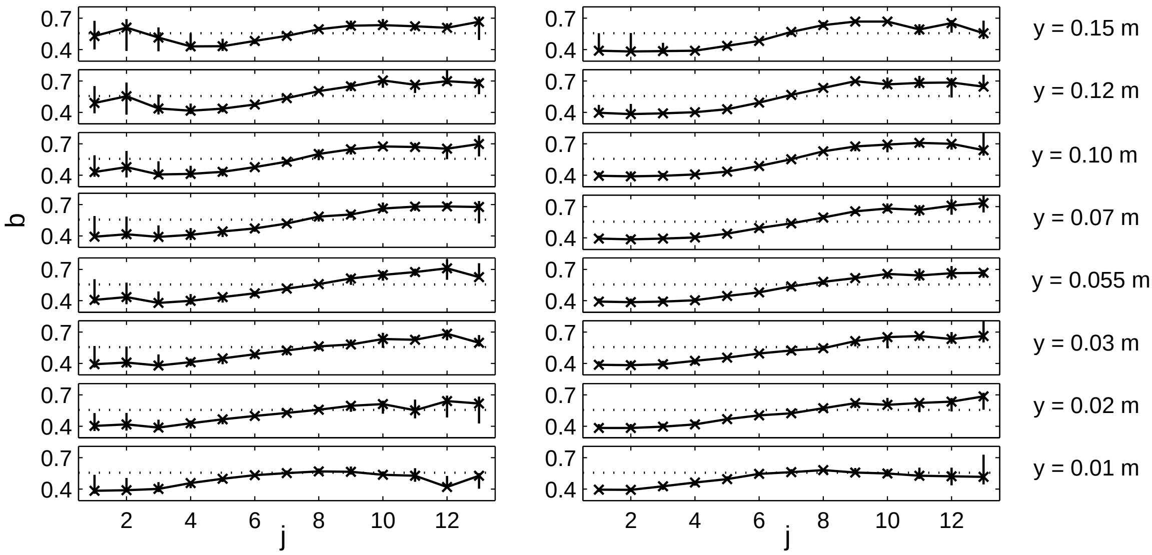

FIG. 6. Median values (asterisk) for the bimodality parameter, b, as a function of scale (abscissa), y (vertical ordering of panels) and U (left-hand panels for U = 6m s^{-1} and right-hand panels for U = 8m s^{-1}). About each point is a vertical line extending from the minimum to the maximum values from the five replicates. These are barely visible in most instances, indicating the replicabiliy of the results. The horizontal dotted line at $b = 5/9$ shows the value for an exponential and a uniform distribution.

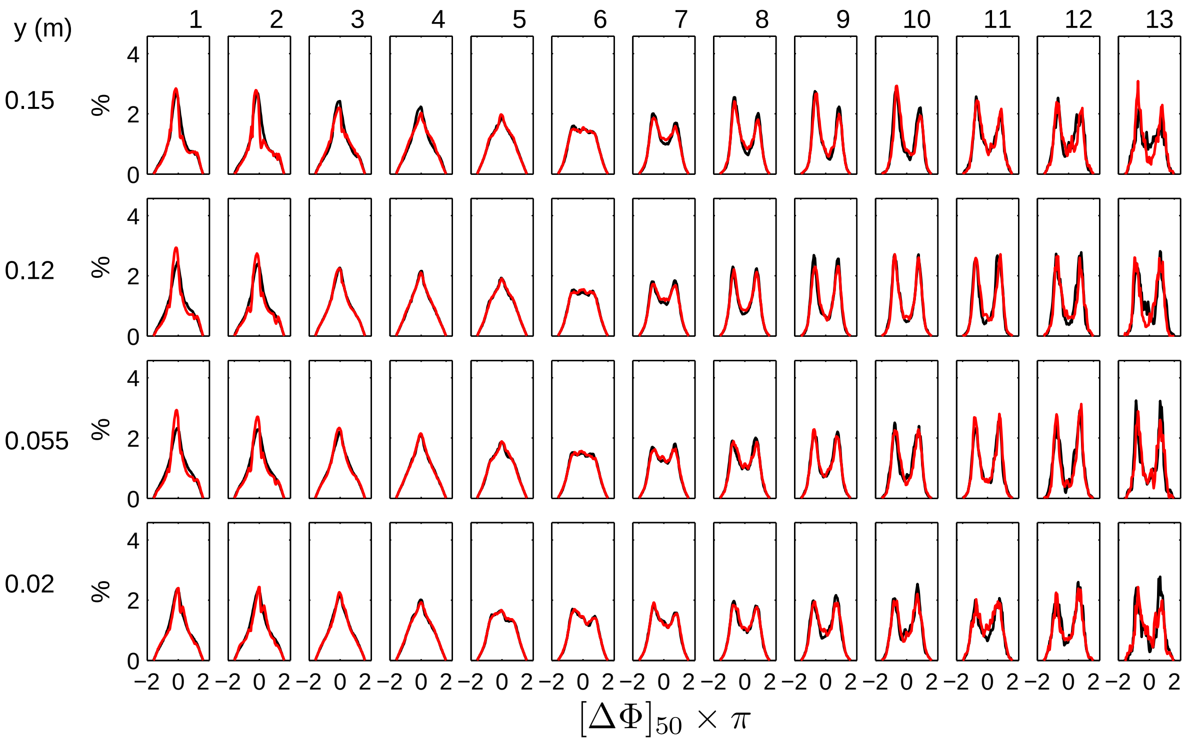

FIG. 7. The median phase difference histograms, $[\Delta\phi(t)]_{50}$, for four choices of y and thirteen choices of j. Results for U = 8 m s^{-1} are shown in black and for U = 6 m s^{-1} are in red. The number above the top row of panels gives the value for j.

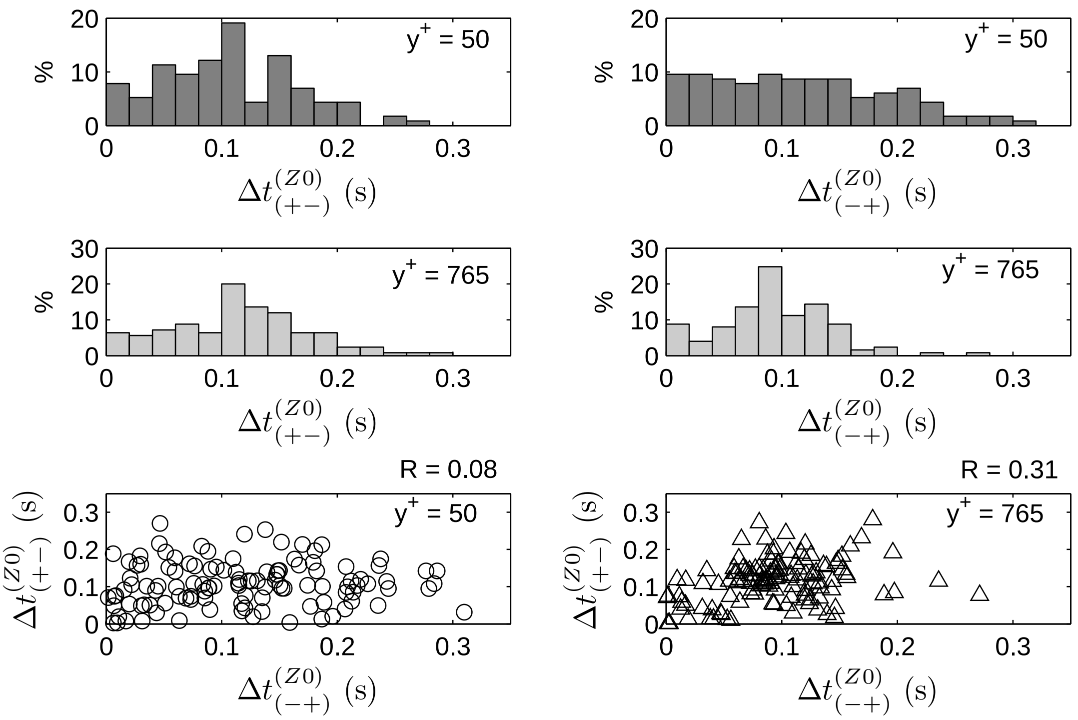

FIG. 8. An analysis of properties of the zero crossings of $\Delta\phi(t)$ series for $U = 6$ ms^{-1} and $j = 10$ at $y = 0.01$ m and $y = 0.15$ m ($y^+ \in \{50, 765\}$). The histograms show results for the time separation, Δt, between the positive-to-negative zero crossings, $\Delta t^{(Z0)}_{(+-)}$ and the negative-to-positive zero crossings, $\Delta t^{(Z0)}_{(-+)}$. The scatterplots in the bottom row indicate any dependence between $\Delta t^{(Z0)}_{(+-)}$ and $\Delta t^{(Z0)}_{(-+)}$ for the two choices of y^+.

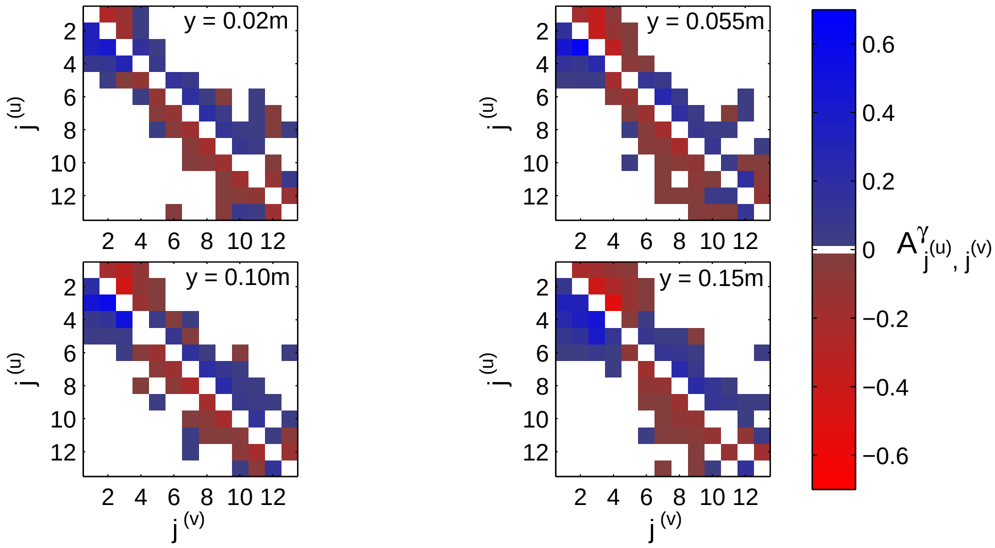

FIG. 9. The asymmetry metric based on median values for γ^* over the five replicates at each $\{j_v, j_u\}$ combination over the five replicates. Results are shown for four choices of y and results plotted above the diagonal are for U = 8 m s^{-1}, with those below for U = 6 m s^{-1}.